MIT Open Access Articles

MCA: A multichannel approach to SAR autofocus

Massachusetts Institute of Technology

MCA: A Multichannel Approach to SAR Autofocus

Robert L. Morrison, Jr., *Member, IEEE*, Minh N. Do, *Senior Member, IEEE*, and David C. Munson, Jr., *Fellow, IEEE*

Abstract—We present a new noniterative approach to synthetic aperture radar (SAR) autofocus, termed the multichannel autofocus (MCA) algorithm. The key in the approach is to exploit the multichannel redundancy of the defocusing operation to create a linear subspace, where the unknown perfectly focused image resides, expressed in terms of a known basis formed from the given defocused image. A unique solution for the perfectly focused image is then directly determined through a linear algebraic formulation by invoking an additional image support condition. The MCA approach is found to be computationally efficient and robust and does not require prior assumptions about the SAR scene used in existing methods. In addition, the vector-space formulation of MCA allows sharpness metric optimization to be easily incorporated within the restoration framework as a regularization term. We present experimental results characterizing the performance of MCA in comparison with conventional autofocus methods and discuss the practical implementation of the technique.

Index Terms—Blind deconvolution, circular deconvolution, image restoration, multichannel, sharpness optimization, signal subspace methods, synthetic aperture radar (SAR) autofocus.

I. INTRODUCTION

IN synthetic aperture radar (SAR) imaging, demodulation timing errors at the radar receiver, due to signal delays resulting from error in the estimated trajectory of the radar platform (i.e., line-of-sight motion perturbations within the slant plane) or from error inserted by signal propagation through the ionosphere, produce unknown phase errors in the Fourier imaging data. As a consequence of the phase errors, the resulting SAR images can be improperly focused. The *SAR Autofocus* problem is concerned with the restoration of the perfectly focused image given the phase-corrupted Fourier data and assumptions about the underlying SAR scene.

In typical SAR data acquisitions, the phase error can be modeled as varying only along one dimension in the Fourier domain. The following mathematical model relates the phase-corrupted Fourier imaging data $\tilde{G}$ to the perfect data G through the 1-D phase error function ϕ_e as [1]

$$\tilde{G}[k,n] = G[k,n]e^{j\phi_e[k]} \tag{1}$$

where the row index $k = 0, 1, \ldots, M - 1$ corresponds to the cross-range frequency index and the column index $n = 0, 1, \ldots, N - 1$ corresponds to the range (spatial-domain) coordinate. The SAR image $\tilde{g}$ is formed by applying an inverse 1-D DFT to each column of $\tilde{G}$: $\tilde{g}[m,n] = DFT_k^{-1}\{\tilde{G}[k,n]\}$. Because the phase error ϕ_e is a 1-D function of k, each column of $\tilde{g}$ has been defocused by the same blurring kernel $b[m] = DFT_k^{-1}\{e^{j\phi_e[k]}\}$ as

$$\tilde{g}[m,n] = g[m,n] \circledast_M b[m] \tag{2}$$

where $\circledast_M$ denotes M-point circular convolution, and g is the perfectly focused image.

The SAR autofocus problem has received much attention (note references [2]–[11]). Most of the existing approaches to autofocus create an estimate of the phase error function $\hat{\phi}_e$, and apply this estimate to the corrupt data to produce a focused restoration. To accurately estimate the phase error, appropriate prior assumptions about the underlying SAR scene are invoked. For example, the widely used Phase Gradient Autofocus (PGA) technique is based on the model of a single target at each range coordinate embedded in white complex Gaussian clutter [1, p. 257], [3] (although, in practice PGA is used for a broader class of imagery). Other autofocus techniques utilize image sharpness metrics, where an optimization routine is employed to determine the phase error estimate that minimizes (or maximizes) a particular metric evaluated on the image intensity [4]–[6]. Commonly utilized metrics include entropy and various powers of the image intensity, which tend to favor sparse images such as collections of point scatterers. While the restoration results obtained using these approaches often are outstanding, the techniques sometimes fail to produce correct restorations [5], [12]. The restorations tend to be inaccurate when the underlying scene is poorly described by the assumed image model.

From the defocusing relationship in (2), we see that there is a multichannel nature to the SAR autofocus problem. Fig. 1 presents this analogy: the columns $g^{[n]}$ of the perfectly focused image g can be viewed as a bank of parallel filters that are excited by a common input signal, which is the blurring kernel b. Thus, there is a similarity to *blind multichannel deconvolution* (BMD) problems in that both the channel responses (i.e., perfectly focused image columns) and input (i.e., blurring kernel) are unknown, and it is desired to reconstruct the channel responses given only the output signals (i.e., defocused image columns) [13]. However, there are two main differences be-

R. L. Morrison, Jr. was with the Department of Electrical and Computer Engineering and the Coordinated Science Laboratory, University of Illinois at Urbana-Champaign, Urbana, IL 61801 USA. He is now with the Massachusetts Institute of Technology Lincoln Laboratory, Lexington, MA 02420 USA (e-mail: rmorrisonjr@ieee.org).

M. N. Do is with the Department of Electrical and Computer Engineering, the Coordinated Science Laboratory and the Beckman Institute, University of Illinois at Urbana-Champaign, Urbana, IL 61801 USA (e-mail: minhdo@uiuc.edu).

D. C. Munson, Jr. is with the Department of Electrical Engineering and Computer Science, University of Michigan, Ann Arbor, MI 48109-2122 USA (e-mail: munson@umich.edu).

Color versions of one or more of the figures in this paper are available online at http://ieeexplore.ieee.org.
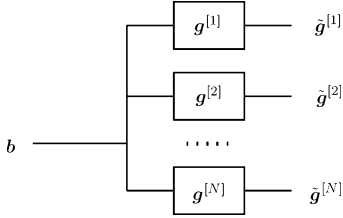
Digital Object Identifier 10.1109/TIP.2009.2012883

Fig. 1. Diagram illustrating the multichannel nature of the autofocus problem. Hffere, b is the blurring kernel, $\{g^{[n]}\}$ are the perfectly focused image columns, and $\{\tilde{g}^{[n]}\}$ are the defocused columns.

tween the SAR autofocus problem considered here and the setup assumed in the BMD literature. First, the filtering operation in the SAR autofocus problem is described by *circular* convolution, as opposed to standard discrete-time convolution. Second, the channel responses $g^{[n]}$, $n = 0, 1, \ldots, N-1$, in the autofocus problem are not short-support FIR filters, but instead have support over the entire signal length. Subspace-based techniques for directly solving for the channel responses have been proposed for the general BMD problem; here, under mild conditions on the channel responses and input, the unknown channel responses are determined exactly (up to a scaling constant) as the solution of a system of linear equations [14], [15]. It is of interest to apply a similar linear algebraic formulation to the SAR autofocus problem, so that the implicit multichannel relationship can be captured explicitly.

In [16], we presented initial results in applying existing subspace-based BMD techniques to the SAR autofocus problem. However, a more efficient and robust approach is to consider the *dual* problem of directly solving for a common focusing operator f (i.e., the inverse of the blurring kernel b), as opposed to solving for all of the channel responses $g^{[n]}$, $n = 0, 1, \ldots, N-1$ [17]. To accomplish this, we explicitly characterize the multichannel condition of the SAR autofocus problem by constructing a low-dimensional subspace where the perfectly focused image resides. The subspace characterization provides a linear framework through which the focusing operator can be directly determined. To determine a unique solution, we assume that a small portion of the perfectly focused image is zero-valued, or corresponds to a region of low return. This constrains the problem sufficiently so that the focusing operator can be obtained as the solution of a known linear system of equations; thus, the solution is determined in a noniterative fashion. We refer to this linear algebraic approach as the *MultiChannel Autofocus* (MCA) algorithm. In practice, the constraint on the underlying image may be enforced approximately by acquiring Fourier-domain data that are sufficiently oversampled in the cross-range dimension, so that the coverage of the image extends beyond the brightly illuminated portion of the scene determined by the antenna pattern [1].

Existing SAR autofocus methods implicitly have relied upon the multichannel condition to properly restore images [18]. In the MCA approach, we have systematically exploited the multichannel condition using an elegant subspace framework. While the success of existing autofocus approaches requires accurate prior assumptions about the underlying scene, such as the suitability of sharpness metrics or knowledge of point scatterers,

MCA does not require prior assumptions about the scene characteristics. The MCA approach is found to be computationally efficient, and robust in the presence of noise and deviations from the image support assumption. In addition, the performance of the proposed technique does not depend on the nature of the phase error; in previous SAR autofocus techniques that do not explicitly exploit the linear structure of the problem, the performance sometimes suffers considerably when the phase errors are large and rapidly varying. MCA is simply expressed in a vector-space framework, allowing sharpness metric optimization to be easily incorporated as a regularization term, and enabling SAR autofocus to be cast into a more unified paradigm with other image restoration problems.

The organization of the paper is as follows. Section II presents the SAR autofocus problem statement, and establishes the notation used in this paper. In Section III, a linear algebraic framework is derived for the problem, and the MCA image restoration procedure is formulated. An analysis of the MCA technique, and its computationally efficient implementation, are presented in Section IV. Section V addresses incorporation of sharpness metric optimization within the MCA restoration framework as a regularization procedure. In Section VI, the application of MCA in practical scenarios is discussed. Section VII presents simulation results using synthetic and actual SAR images. The performance of the proposed technique is compared with that of conventional autofocus algorithms; MCA is found to offer restoration quality on par with, or often superior to, the best existing autofocus approaches.

II. PROBLEM SETUP

Notation

We introduce vector notation for discrete signals. The column vector $b \in \mathbb{C}^M$ is composed of the values of $b[m]$, $m = 0, 1, \ldots, M - 1$. Column n of $g[m, n]$, representing a particular range coordinate of a SAR image, is denoted by the vector $g^{[n]} \in \mathbb{C}^M$. We define $\mathbf{vec}\{g\} \in \mathbb{C}^{MN}$ to be the vector composed of the concatenated columns $g^{[n]}$, $n = 0, 1, \ldots, N - 1$. The notation $\{A\}_\Omega$ refers to the matrix formed from a subset of the rows of A, where Ω is a set of row indices. Lastly, $C\{b\} \in \mathbb{C}^{M \times M}$ is a circulant matrix formed with the vector b

$$C\{b\} = \begin{bmatrix} b[0] & b[M-1] & \ldots & b[1] \\ b[1] & b[0] & \ldots & b[2] \\ \vdots & \vdots & \ddots & \vdots \\ b[M-1] & b[M-2] & \ldots & b[0] \end{bmatrix}. \quad (3)$$

A. Problem Description and Characterization of the Solution Space

The aim of *SAR autofocus* is to restore the perfectly focused image g given the defocused image $\tilde{g}$ and assumptions about the characteristics of the underlying scene. Using (1) and (2), the defocusing relationship in the spatial-domain is expressed as

$$\tilde{g} = \underbrace{F^H D(e^{j\phi_e}) F}_{C\{b\}} g \quad (4)$$

where $\boldsymbol{F} \in \mathbb{C}^{M \times M}$ is the 1-D DFT unitary matrix with entries $F_{k,m} = 1/\sqrt{M} e^{-j2\pi km/M}$, $\boldsymbol{F}^H$ is the Hermitian of $\boldsymbol{F}$ and represents the inverse DFT, $\boldsymbol{D}(e^{j\phi_e}) \in \mathbb{C}^{M \times M}$ is a diagonal matrix with the entries $e^{j\phi_e[k]}$ on the diagonal, and $\boldsymbol{C}\{\boldsymbol{b}\} \in \mathbb{C}^{M \times M}$ is a circulant matrix formed with the blurring kernel $\boldsymbol{b}$, where $b[m] = DFT_k^{-1}\{e^{j\phi_e[k]}\}$. Thus, the defocusing effect can be described as the multiplication of the perfectly focused image by a circulant matrix with eigenvalues equal to the unknown phase errors. Likewise, we define the *solution space* to be the set of all images formed from $\tilde{\boldsymbol{g}}$ with different $\boldsymbol{\phi}$

$$\hat{\boldsymbol{g}}(\boldsymbol{\phi}) = \underbrace{\boldsymbol{F}^H \boldsymbol{D}(e^{-j\boldsymbol{\phi}}) \boldsymbol{F} \tilde{\boldsymbol{g}}}_{C\{\boldsymbol{f}_A\}} \qquad (5)$$

where $\boldsymbol{f}_A$ is an *all-pass* correction filter. Note that $\hat{\boldsymbol{g}}(\boldsymbol{\phi}_e) = \boldsymbol{g}$.

Autofocus algorithms typically solve for the *phase error estimate* $\hat{\phi}$ directly, and apply this to the corrupt imaging data $\tilde{G}$ to restore the image

$$\hat{g}[m,n] = DFT_k^{-1}\{\tilde{G}[k,n] e^{-j\hat{\phi}[k]}\}. \qquad (6)$$

Most SAR autofocus methods are iterative, evaluating some measure of quality in the spatial domain and then perturbing the estimate of the Fourier phase error function in a manner that increases the image focus. In this paper, we present a non-iterative approach where a focusing operator $\boldsymbol{f}$ is directly determined to restore the image; given $\boldsymbol{f}$, it is straightforward to obtain $\hat{\phi} = \phi_e$. Underlying the approach is a linear subspace characterization for the problem, which allows the focusing operator to be computed using a linear algebraic formulation. This is addressed in the next section.

III. MCA RESTORATION FRAMEWORK

A. Explicit Multichannel Condition

Our goal is to create a *subspace* for the perfectly focused image $\boldsymbol{g}$, spanned by a basis constructed from the given defocused image $\tilde{\boldsymbol{g}}$. To accomplish this, we generalize the relationship in (5) to include *all* correction filters $\boldsymbol{f} \in \mathbb{C}^M$, that is, not just the subset of allpass correction filters $\boldsymbol{f}_A$. As a result, for a given defocused image $\tilde{\boldsymbol{g}}$, we obtain an M-dimensional subspace where the perfectly focused image $\boldsymbol{g}$ lives

$$\hat{\boldsymbol{g}}(\boldsymbol{f}) = C\{\boldsymbol{f}\}\tilde{\mathrm{g}} \qquad (7)$$

where $\hat{\boldsymbol{g}}(\boldsymbol{f})$ denotes the restoration formed by applying $\boldsymbol{f}$. This subspace characterization explicitly captures the *multichannel condition* of SAR autofocus: the assumption that each column of the image is defocused by the same blurring kernel.

To produce a basis expansion for the subspace in terms of $\tilde{\boldsymbol{g}}$, we select the standard basis $\{\boldsymbol{e}_k\}_{k=0}^{M-1}$ for $\mathbb{C}^M$, i.e., $\boldsymbol{e}_k[m] = 1$ if $m = k$ and 0 otherwise, and express the correction filter as

$$\boldsymbol{f} = \sum_{k=0}^{M-1} f_k \boldsymbol{e}_k. \qquad (8)$$

Note that at this point we do not enforce the allpass condition; the advantage of generalizing to all $\boldsymbol{f} \in \mathbb{C}^M$ is to create a linear

framework. Using the linearity property of circular convolution, we have

$$C\{\boldsymbol{f}\} = \sum_{k=0}^{M-1} f_k C\{\boldsymbol{e}_k\}.$$

From this, any image $\hat{\boldsymbol{g}}$ in the subspace can be expressed in terms of a basis expansion as

$$\hat{\boldsymbol{g}}(\boldsymbol{f}) = \sum_{k=0}^{M-1} f_k \boldsymbol{\varphi}^{[k]}(\tilde{\boldsymbol{g}}) \qquad (9)$$

where

$$\boldsymbol{\varphi}^{[k]}(\tilde{\boldsymbol{g}}) = C\{\boldsymbol{e}_k\}\tilde{\boldsymbol{g}} \qquad (10)$$

are known basis functions (since $\tilde{\boldsymbol{g}}$ is given) for the M-dimensional subspace containing the unknown perfectly focused image $\boldsymbol{g}$. In matrix form, we can write (9) as

$$\mathbf{vec}\{\hat{\boldsymbol{g}}(\boldsymbol{f})\} = \boldsymbol{\Phi}(\tilde{\boldsymbol{g}})\boldsymbol{f} \qquad (11)$$

where

$$\boldsymbol{\Phi}(\tilde{\boldsymbol{g}}) \stackrel{\mathrm{def}}{=} [\mathbf{vec}\{\boldsymbol{\varphi}^{[0]}(\tilde{\boldsymbol{g}})\}, \mathbf{vec}\{\boldsymbol{\varphi}^{[1]}(\tilde{\boldsymbol{g}})\},$$
$$\dots, \mathbf{vec}\{\boldsymbol{\varphi}^{[M-1]}(\tilde{\boldsymbol{g}})\}] \quad (12)$$

is referred to as the *basis matrix*. Note that for there to be a unique solution for $\boldsymbol{f}$, $\boldsymbol{\Phi}(\tilde{\boldsymbol{g}})$ must have rank M. We explore conditions on the rank of the defocused image $\tilde{\boldsymbol{g}}$ in more detail in Section IV.

B. MCA Direct Solution Approach

To formulate the MCA approach, we express the unknown perfectly focused image in terms of the basis expansion in (9)

$$\mathbf{vec}\{\boldsymbol{g}\} = \boldsymbol{\Phi}(\tilde{\boldsymbol{g}})\boldsymbol{f}^\star \qquad (13)$$

where $\boldsymbol{f}^\star$ is the true correction filter satisfying $\hat{\boldsymbol{g}}(\boldsymbol{f}^\star) = \boldsymbol{g}$. Here, the matrix $\boldsymbol{\Phi}(\tilde{\boldsymbol{g}})$ is known, but $\boldsymbol{g}$ and $\boldsymbol{f}^\star$ are unknown. By imposing an image support constraint on the perfectly focused image $\boldsymbol{g}$, the linear system in (13) can be constrained sufficiently so that the unknown correction filter $\boldsymbol{f}^\star$ can be directly solved for. Specifically, we assume that $\boldsymbol{g}$ is approximately zero-valued over a particular set of *low-return* pixels Ω

$$g[m,n] = \begin{cases} \xi[m,n], & \text{for } m,n \in \Omega \\ g'[m,n], & \text{for } m,n \notin \Omega \end{cases} \qquad (14)$$

where $\xi[m,n]$ are low-return pixels ($|\xi[m,n]| \approx 0$) and $g'[m,n]$ are unknown nonzero pixels. We define $\bar{\Omega}$ to be the set of nonzero pixels (i.e., the complement of Ω), and we say that these pixels correspond to the *region of support* (ROS). In practice, the desired image support condition can be achieved by exploiting the spatially limited illumination of the antenna beam, or by using prior knowledge of low-return regions in the SAR image. We will elaborate more on the practical application of the image support assumption in Section VI.

Enforcing spatially limited constraint (14) directly into multichannel framework, (13) becomes

$$\begin{bmatrix} \boldsymbol{\xi} \\ \mathbf{vec}\{\boldsymbol{g'}\} \end{bmatrix} = \begin{bmatrix} \{\boldsymbol{\Phi}(\tilde{\boldsymbol{g}})\}_\Omega \\ \{\boldsymbol{\Phi}(\tilde{\boldsymbol{g}})\}_{\bar{\Omega}} \end{bmatrix} \boldsymbol{f}^\star \tag{15}$$

where $\boldsymbol{\xi} = \{\mathbf{vec}\{\boldsymbol{g}\}\}_\Omega$ is a vector of the low-return *constraints*, $\{\boldsymbol{\Phi}(\tilde{\boldsymbol{g}})\}_\Omega$ are the rows of $\boldsymbol{\Phi}(\tilde{\boldsymbol{g}})$ that correspond to the low-return constraints, and $\{\boldsymbol{\Phi}(\tilde{\boldsymbol{g}})\}_{\bar{\Omega}}$ are the rows of $\boldsymbol{\Phi}(\tilde{\boldsymbol{g}})$ that correspond to the unknown pixel values of $\boldsymbol{g}$ within the ROS. Given that $\boldsymbol{\xi}$ has dimension $M-1$ or greater (i.e., there are at least $M-1$ zero constraints), when $\boldsymbol{\xi} = \boldsymbol{0}$ the correction filter $\boldsymbol{f}^\star$ can be uniquely determined up to a scaling constant by solving for $\boldsymbol{f}$ in

$$\{\boldsymbol{\Phi}(\tilde{\boldsymbol{g}})\}_\Omega \boldsymbol{f} = \boldsymbol{0}. \tag{16}$$

We denote this direct linear solution method for determining the correction filter as the *MultiChannel Autofocus* (MCA) approach, and define

$$\boldsymbol{\Phi}_\Omega(\tilde{\boldsymbol{g}}) \stackrel{\text{def}}{=} \{\boldsymbol{\Phi}(\tilde{\boldsymbol{g}})\}_\Omega$$

to be the *MCA matrix* formed using the constraint set Ω.

Given the assumption $\boldsymbol{\xi} = \boldsymbol{0}$, the MCA approach requires that $\boldsymbol{\Phi}_\Omega(\tilde{\boldsymbol{g}})$ is a rank $M-1$ matrix (note that $\boldsymbol{\Phi}_\Omega(\tilde{\boldsymbol{g}})$ is a matrix formed from a *subset* of the rows of the basis matrix $\boldsymbol{\Phi}(\tilde{\boldsymbol{g}})$ and, thus, will have rank less than or equal to M). In Section IV, we state the necessary conditions for which this rank condition is satisfied. The solution $\hat{\boldsymbol{f}}$ to (16) can be obtained by determining the unique vector spanning the nullspace of $\boldsymbol{\Phi}_\Omega(\tilde{\boldsymbol{g}})$ as

$$\hat{\boldsymbol{f}} = \text{Null}(\boldsymbol{\Phi}_\Omega(\tilde{\boldsymbol{g}})) = \alpha \boldsymbol{f}^\star \tag{17}$$

where α is an arbitrary complex constant. To eliminate the magnitude scaling α, we use the Fourier phase of $\hat{\boldsymbol{f}}$ to correct the defocused image according to (6)

$$\hat{\phi}[k] = -\angle\left(DFT_m\{\hat{f}[m]\}\right). \tag{18}$$

In other words, we enforce the allpass condition of $\hat{\boldsymbol{f}}$ to determine a unique solution from (17).

C. Restoration Using the SVD

When $|\xi[m,n]| \neq 0$ in (14), or when the defocused image is contaminated by additive noise, the MCA matrix has full column rank. In this case, we cannot obtain $\hat{\boldsymbol{f}}$ as the null vector of $\boldsymbol{\Phi}_\Omega(\tilde{\boldsymbol{g}})$. However, by performing the singular value decomposition (SVD) of $\boldsymbol{\Phi}_\Omega(\tilde{\boldsymbol{g}})$, a unique vector that produces the minimum gain solution (in the ℓ_2-sense) can be determined. We express the SVD as

$$\boldsymbol{\Phi}_\Omega(\tilde{\boldsymbol{g}}) = \tilde{\boldsymbol{U}}\tilde{\boldsymbol{\Sigma}}\tilde{\boldsymbol{V}}^H \tag{19}$$

where $\tilde{\boldsymbol{\Sigma}} = \text{diag}(\sigma_1, \sigma_2, \ldots, \sigma_M)$ is a diagonal matrix of the singular values satisfying $\sigma_1 \geq \sigma_2 \geq \cdots \geq \sigma_M \geq 0$. Since $\boldsymbol{f}$ is an allpass filter we have $\|\boldsymbol{f}\|_2 = 1$. Although we can no longer assume the pixels in the low-return region to be exactly zero, it

is reasonable to require the low-return region to have minimum energy subject to $\|\boldsymbol{f}\|_2 = 1$. A solution $\hat{\boldsymbol{f}}$ satisfying

$$\hat{\boldsymbol{f}} = \arg\min_{\|\boldsymbol{f}\|_2 = 1} \|\boldsymbol{\Phi}_\Omega(\tilde{\boldsymbol{g}})\boldsymbol{f}\|_2 \tag{20}$$

is given by $\hat{\boldsymbol{f}} = \tilde{\boldsymbol{V}}^{[M]}$, which is the right singular vector corresponding to the smallest singular value of $\boldsymbol{\Phi}_\Omega(\tilde{\boldsymbol{g}})$ [19].

IV. PERFORMANCE ANALYSIS

A. General Properties of $\boldsymbol{\Phi}_\omega(\tilde{\boldsymbol{g}})$

A key observation underlying the success of the MCA approach is that the circulant blurring matrix $\boldsymbol{C}\{\boldsymbol{b}\}$ is unitary. This result is arrived at using (4), where all the eigenvalues of $\boldsymbol{C}\{\boldsymbol{b}\}$ are observed to have unit magnitude, and the fact that the DFT matrix $\boldsymbol{F}$ is unitary, as follows:

$$\boldsymbol{C}\{\boldsymbol{b}\}\boldsymbol{C}^H\{\boldsymbol{b}\} = \boldsymbol{F}^H \boldsymbol{D}(e^{j\phi_e})\boldsymbol{F}\boldsymbol{F}^H \boldsymbol{D}(e^{-j\phi_e})\boldsymbol{F} = \boldsymbol{I}. \tag{21}$$

We observe that the basis matrix $\boldsymbol{\Phi}(\tilde{\boldsymbol{g}})$ has a special structure by rewriting (7) for a single column as

$$\hat{g}^{[n]}(\boldsymbol{f}) = \boldsymbol{f} \circledast_M \tilde{g}^{[n]} = \boldsymbol{C}\{\tilde{g}^{[n]}\}\boldsymbol{f}. \tag{22}$$

Comparing with (11), where the left side of the equation is formed by stacking the column vectors $\hat{g}^{[n]}(\boldsymbol{f})$, and using (22), we have

$$\boldsymbol{\Phi}(\tilde{\boldsymbol{g}}) = \begin{bmatrix} \boldsymbol{C}\{\tilde{g}^{[0]}\} \\ \boldsymbol{C}\{\tilde{g}^{[1]}\} \\ \vdots \\ \boldsymbol{C}\{\tilde{g}^{[N-1]}\} \end{bmatrix}. \tag{23}$$

Analogous to (12), we define $\boldsymbol{\Phi}(\boldsymbol{g})$ to be the basis matrix formed by the perfectly focused image $\boldsymbol{g}$, i.e., $\boldsymbol{\Phi}(\boldsymbol{g})$ is formed by using $\boldsymbol{g}$ instead of $\tilde{\boldsymbol{g}}$ in (12). Likewise, $\boldsymbol{\Phi}_\Omega(\boldsymbol{g}) = \{\boldsymbol{\Phi}(\boldsymbol{g})\}_\Omega$ is the MCA matrix formed from the perfectly focused image. From the unitary property of $\boldsymbol{C}\{\boldsymbol{b}\}$, we establish the following result.

Proposition 1 (Equivalence of Singular Values): Suppose that $\tilde{\boldsymbol{g}} = \boldsymbol{C}\{\boldsymbol{b}\}\boldsymbol{g}$. Then, $\boldsymbol{\Phi}_\Omega(\tilde{\boldsymbol{g}}) = \boldsymbol{\Phi}_\Omega(\mathrm{g})\boldsymbol{C}\{\boldsymbol{b}\}$ and the singular values of $\boldsymbol{\Phi}_\Omega(\boldsymbol{g})$ and $\boldsymbol{\Phi}_\Omega(\tilde{\boldsymbol{g}})$ are identical.

Proof: From the assumption, $\tilde{g}^{[n]} = \boldsymbol{b} \circledast_M g^{[n]}$. Therefore, $\boldsymbol{C}\{\tilde{g}^{[n]}\} = \boldsymbol{C}\{g^{[n]}\}\boldsymbol{C}\{\boldsymbol{b}\}$, and from (23)

$$\boldsymbol{\Phi}(\tilde{\boldsymbol{g}}) = \begin{bmatrix} \boldsymbol{C}\{g^{[0]}\}\boldsymbol{C}\{\boldsymbol{b}\} \\ \boldsymbol{C}\{g^{[1]}\}\boldsymbol{C}\{\boldsymbol{b}\} \\ \vdots \\ \mathrm{C}\{g^{[N-1]}\}\boldsymbol{C}\{\boldsymbol{b}\} \end{bmatrix} = \boldsymbol{\Phi}(\boldsymbol{g})\boldsymbol{C}\{\boldsymbol{b}\}. \tag{24}$$

Note that (24) implies that $\{\boldsymbol{\Phi}(\tilde{\boldsymbol{g}})\}_\Omega = \{\boldsymbol{\Phi}(\boldsymbol{g})\}_\Omega \boldsymbol{C}\{\boldsymbol{b}\}$. As a result

$$\begin{aligned} \boldsymbol{\Phi}_\Omega(\tilde{\boldsymbol{g}})\boldsymbol{\Phi}_\Omega^H(\tilde{\boldsymbol{g}}) &= \boldsymbol{\Phi}_\Omega(\boldsymbol{g})\boldsymbol{C}\{\boldsymbol{b}\}\boldsymbol{C}^H\{\boldsymbol{b}\}\boldsymbol{\Phi}_\Omega^H(\boldsymbol{g}) \\ &= \boldsymbol{\Phi}_\Omega(\boldsymbol{g})\boldsymbol{\Phi}_\Omega^H(\boldsymbol{g}) \end{aligned}$$

and, thus, $\boldsymbol{\Phi}_\Omega(\boldsymbol{g})$ and $\boldsymbol{\Phi}_\Omega(\tilde{\boldsymbol{g}})$ have the same singular values. $\square$

Thus, from Proposition 1, we can write the SVD of the MCA matrices for $\boldsymbol{g}$ and $\tilde{\boldsymbol{g}}$ as $\boldsymbol{\Phi}_\Omega(\boldsymbol{g}) = \boldsymbol{U}\boldsymbol{\Sigma}\boldsymbol{V}^H$ and $\boldsymbol{\Phi}_\Omega(\tilde{\boldsymbol{g}}) = \tilde{\boldsymbol{U}}\boldsymbol{\Sigma}\tilde{\boldsymbol{V}}^H$, respectively. The following result demonstrates that the MCA restoration obtained through $\boldsymbol{\Phi}_\Omega(\tilde{\boldsymbol{g}})$ and $\tilde{\boldsymbol{g}}$ is the same as the restoration obtained using $\boldsymbol{\Phi}_\Omega(\boldsymbol{g})$ and $\boldsymbol{g}$.

Proposition 2 (Equivalance of Restorations): Suppose that $\boldsymbol{\Phi}_\Omega(\boldsymbol{g})$ (or equivalently $\boldsymbol{\Phi}_\Omega(\tilde{\boldsymbol{g}})$) has a distinct smallest singular value. Then applying the MCA correction filters $\boldsymbol{V}^{[M]}$ and $\tilde{\boldsymbol{V}}^{[M]}$ to $\boldsymbol{g}$ and $\tilde{\boldsymbol{g}}$, respectively, produce the same restoration in absolute values; i.e.,

$$\left| \boldsymbol{C}\{\tilde{\boldsymbol{V}}^{[M]}\}\tilde{\boldsymbol{g}} \right| = \left| \boldsymbol{C}\{\boldsymbol{V}^{[M]}\}\boldsymbol{g} \right|. \tag{25}$$

Proof: Expressing $\boldsymbol{\Phi}_\Omega(\tilde{\boldsymbol{g}}) = \boldsymbol{\Phi}_\Omega(\mathrm{g})\boldsymbol{C}\{\boldsymbol{b}\}$ in terms of the SVD of $\boldsymbol{\Phi}_\Omega(\boldsymbol{g})$ and $\boldsymbol{\Phi}_\Omega(\tilde{\boldsymbol{g}})$, we have

$$\boldsymbol{\Phi}_\Omega(\tilde{\boldsymbol{g}}) = \tilde{\boldsymbol{U}}\boldsymbol{\Sigma}\tilde{\boldsymbol{V}}^H = \boldsymbol{U}\boldsymbol{\Sigma}\boldsymbol{V}^H\boldsymbol{C}\{\boldsymbol{b}\}. \tag{26}$$

Because of the assumption in the proposition, the right singular vector corresponding to the smallest singular value of $\boldsymbol{\Phi}_\Omega(\tilde{\boldsymbol{g}})$ is uniquely determined to within a constant scalar factor β of absolute value one [19]

$$\tilde{\boldsymbol{V}}^{[M]H} = \beta \boldsymbol{V}^{[M]H}\boldsymbol{C}\{\boldsymbol{b}\} \tag{27}$$

where $|\beta| = 1$. Taking the transpose of both sides of (27) produces $\tilde{\boldsymbol{V}}^{[M]} = \beta^* \boldsymbol{C}^H\{\boldsymbol{b}\}\boldsymbol{V}^{[M]}$. Using the unitary property of $\boldsymbol{C}\{\boldsymbol{b}\}$

$$\boldsymbol{V}^{[M]} = \beta^{*-1}\boldsymbol{C}\{\boldsymbol{b}\}\tilde{\boldsymbol{V}}^{[M]}. \tag{28}$$

We then have

$$\begin{aligned} \boldsymbol{C}\{\boldsymbol{V}^{[M]}\}\boldsymbol{g} &= \beta^{*-1}\boldsymbol{C}\{\boldsymbol{b}\}\boldsymbol{C}\{\tilde{\boldsymbol{V}}^{[M]}\}\boldsymbol{g} \\ &= \beta^{*-1}\boldsymbol{C}\{\tilde{\boldsymbol{V}}^{[M]}\}\boldsymbol{C}\{\boldsymbol{b}\}\boldsymbol{g} \\ &= \beta^{*-1}\boldsymbol{C}\{\tilde{\boldsymbol{V}}^{[M]}\}\tilde{\boldsymbol{g}} \end{aligned}$$

and, thus, $\boldsymbol{C}\{\boldsymbol{V}^{[M]}\}\boldsymbol{g}$ and $\boldsymbol{C}\{\tilde{\boldsymbol{V}}^{[M]}\}\tilde{\boldsymbol{g}}$ have the same absolute value since $|\beta^{*-1}| = 1$. $\square$

Proposition 2 is useful for two reasons. First, it demonstrates that applying MCA to the perfectly focused image or any defocused image described by (4) produces the same restored image magnitude, and also produces the same restored phase to within the phase offset $\angle\beta^{*-1}$ (which is constant over the entire image). In other words, the restoration formed using the MCA approach does not depend on the phase error function; the MCA restoration depends only on $\boldsymbol{g}$ and the selection of low-return constraints Ω (i.e., the pixels in $\boldsymbol{g}$ we are assuming to be low-return). This finding is significant because existing autofocus techniques tend to perform less well when the phase errors are large and rapidly varying [1], [12]. We note that while the MCA restoration is the same under any phase error function, this result does not imply anything about the quality of the restoration. Second, Proposition 2 shows that it is sufficient to examine the perfectly focused image to determine the conditions under which unique restorations are possible using MCA.
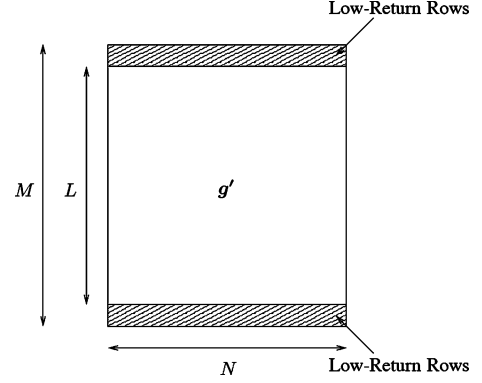

Fig. 2. Illustration of the spatially limited image support assumption in the special case where there are low-return rows in the perfectly focused image.

B. Special Case: Low-Return Rows

A case of particular interest is where Ω corresponds to a set of low-return rows. The consideration of row constraints matches a practical case of interest where the attenuation due to the antenna pattern is used to satisfy the low-return pixel assumption (this is addressed in Section VI). In this case, $\boldsymbol{\Phi}_\Omega(\boldsymbol{g})$ has special structure that can be exploited for efficient computation. This form also allows the necessary conditions for a unique correction filter to be precisely determined.

Fig. 2 shows an illustration of the special case, where there are L rows within the ROS, and the top and bottom rows are low-return. We define the set $\mathcal{L} = \{l_1, l_2, \ldots, l_R\}$ to be the set of low-return row indices, where $R = M - L$ is the number of low-return rows and $0 \leq l_j \leq M - 1$, such that

$$g[m,n] = \begin{cases} \xi[m,n], & \text{for } m \in \mathcal{L} \\ g'[m,n], & \text{for } m \notin \mathcal{L}. \end{cases} \tag{29}$$

To explicitly construct the MCA matrix in this case, we first use (7) to express

$$\boldsymbol{g}^T = \tilde{\boldsymbol{g}}^T \boldsymbol{C}^T\{\boldsymbol{f}^\star\} \tag{30}$$

where T denotes transpose. We consider the transposed images because this allows us to represent the low-return rows in $\boldsymbol{g}$ as column vectors, which leads to an expression of the form (16) where $\boldsymbol{\Phi}_\Omega(\tilde{\boldsymbol{g}})$ is explicitly defined. Note that

$$\boldsymbol{C}^T\{\boldsymbol{f}\} = [\boldsymbol{f}_F, \boldsymbol{C}\{\boldsymbol{e}_1\}\boldsymbol{f}_F, \ldots, \boldsymbol{C}\{\boldsymbol{e}_{M-1}\}\boldsymbol{f}_F] \tag{31}$$

where $\boldsymbol{C}\{\boldsymbol{e}_l\}$ is the l-component circulant shift matrix, and

$$f_F[m] = f[\langle -m \rangle_M] \tag{32}$$

$m = 0, 1, \ldots, M - 1$, is a flipped version of the true correction filter ($\langle n \rangle_M$ denotes n modulo M). Using (30) and (31), we express the lth row of $\boldsymbol{g}$ as

$$(\boldsymbol{g}^T)^{[l]} = \tilde{\boldsymbol{g}}^T \boldsymbol{C}\{\boldsymbol{e}_l\}\boldsymbol{f}_F^\star. \tag{33}$$

Note that multiplication with the matrix $\boldsymbol{C}\{\boldsymbol{e}_l\}$ in the expression above results in an l-component left circulant shift along each row of $\tilde{\boldsymbol{g}}^T$.

The relationship in (33) is informative because it shows how the MCA matrix $\boldsymbol{\Phi}_\Omega(\tilde{g})$ can be constructed given the image support constraint in (29). For the low-return rows satisfying $(\boldsymbol{g}^T)^{[l_j]} \approx \boldsymbol{0}$, we have the relation

$$(\boldsymbol{g}^T)^{[l_j]} = \tilde{\boldsymbol{g}}^T C\{e_{l_j}\} \boldsymbol{f}_F^\star \approx 0 \qquad (34)$$

for $j = 1, 2, \ldots, R$. Enforcing (34) for all of the low-return rows simultaneously produces

$$\boldsymbol{0} \approx \underbrace{\begin{bmatrix} \tilde{\boldsymbol{g}}^T C\{e_{l_1}\} \\ \tilde{\boldsymbol{g}}^T C\{e_{l_2}\} \\ \vdots \\ \tilde{\boldsymbol{g}}^T C\{e_{l_R}\} \end{bmatrix}}_{\boldsymbol{\Phi}_\mathcal{L}(\tilde{g})} \boldsymbol{f}_F^\star \qquad (35)$$

where (with abuse of notation) $\boldsymbol{\Phi}_\mathcal{L}(\tilde{g}) \in \mathbb{C}^{NR \times M}$ is the MCA matrix for the row constraint set $\mathcal{L}$. In this special case, $\boldsymbol{\Phi}_\mathcal{L}$ plays the same role as $\boldsymbol{\Phi}_\Omega$ for the general case. Thus, we see that in this case the MCA matrix is formed by stacking shifted versions of the transposed defocused image, where the shifts correspond to the locations of the low-return rows in the perfectly focused image. Determining the null vector (or minimum right singular vector) of $\boldsymbol{\Phi}_\mathcal{L}(\tilde{g})$ as defined in (35) produces a flipped version of the correction filter; the correction filter $\boldsymbol{f}$ can be obtained by appropriately shifting the elements of $\boldsymbol{f}_F$ according to (32). The reason for considering the flipped form in (35) is that it provides a special structure for efficiently computing $\boldsymbol{f}$, as we will demonstrate in the next subsection.

To determine necessary conditions for a unique and correct solution of the MCA (16), we restrict our analysis to the model in (29) where the low-return rows are identically zero: $\xi[m, n] = 0$. From Propositions 1 and 2, the conditions for a unique solution to (16) can be determined using $\boldsymbol{\Phi}_\mathcal{L}(g)$ in place of $\boldsymbol{\Phi}_\mathcal{L}(\tilde{g})$. This, in turn, is equivalent to requiring $\boldsymbol{\Phi}_\mathcal{L}(g)$ to be a rank $M-1$ matrix.

Proposition 3 (Necessary Condition for Unique and Correct Solution): Consider the image model $g[m, n] = 0$ for $m \in \mathcal{L}$ and $g[m, n] = g'[m, n]$ for $m \notin \mathcal{L}$. Then a necessary condition for MCA to produce a unique and correct solution to the autofocus problem is

$$\text{rank}(\boldsymbol{g}') \geq \frac{M-1}{R}. \qquad (36)$$

Proof: First notice that

$$\text{rank}(\tilde{\boldsymbol{g}}^T C\{e_{l_j}\}) = \text{rank}(\tilde{\boldsymbol{g}}) = \text{rank}(C\{b\}g)$$
$$= \text{rank}(\boldsymbol{g}) = \text{rank}(\boldsymbol{g}'))$$

because $C\{e_{l_j}\}$ and $C\{b\}$ are unitary matrices, and the zero-row assumption of the image $\boldsymbol{g}$. Then from (35), we have

$$\text{rank}(\boldsymbol{\Phi}_\mathcal{L}(\tilde{g})) \leq R \, \text{rank}(\boldsymbol{g}').$$

Therefore, a necessary condition for $\text{rank}(\boldsymbol{\Phi}_\mathcal{L}(\tilde{g})) = M-1$ is $\text{rank}(\boldsymbol{g}') \geq (M-1)/R$. Furthermore, notice that the filter $\boldsymbol{f}_{Id} \stackrel{\text{def}}{=} [1, 0, \ldots, 0]^T$ is always a solution to (16) for $\boldsymbol{g}$ as defined in the proposition statement: $\boldsymbol{\Phi}_\mathcal{L}(g)\boldsymbol{f}_{Id} = \boldsymbol{0}$. This is because applying $\boldsymbol{f}_{Id}$ to $\boldsymbol{g}$ returns the same image $\boldsymbol{g}$, where all the

pixels in the low-return region are zero by assumption. Thus, the unique solution for (16) is also the correct solution to the autofocus problem. $\qquad \square$

Noting that $M = R + L$, and using condition (36), we derive the minimum number of zero-return rows R required to achieve a unique solution as a function of the rank of $\boldsymbol{g}'$

$$R \geq \frac{L-1}{\text{rank}(\boldsymbol{g}') - 1}. \qquad (37)$$

The condition $\text{rank}(\boldsymbol{g}') = \min(L, N)$ usually holds, with the exception of degenerate cases where the rows or columns of $\boldsymbol{g}'$ are linearly dependent. Since $\text{rank}(\boldsymbol{g}') \leq \min(L, N)$, (37) implies

$$R \geq \frac{L-1}{\min(L, N) - 1}. \qquad (38)$$

The condition in (38) provides a rule for determining the minimum R (the minimum number of low-return rows required) as a function of the dimensions of the ROS in the general case where $\xi[n, m] \neq 0$.

C. Efficient Restoration Procedure

Forming the MCA matrix according to (35) and performing its full SVD can be computationally expensive in terms of both memory and CPU time when there are many low-return rows, since the dimensions of $\boldsymbol{\Phi}_\mathcal{L}(\tilde{g})$ are NR rows by M columns. As an example, for a 1000 by 1000 pixel image with 100 low-return rows, $\boldsymbol{\Phi}_\mathcal{L}(\tilde{g})$ is a 100000×1000 matrix; in this case, it is not practical to construct and invert such a large matrix.

Due to the structure of $\boldsymbol{\Phi}_\mathcal{L}(\tilde{g})$, it is possible to efficiently compute the minimum right singular vector solution in (20). Note that the right singular vectors of $\boldsymbol{\Phi}_\mathcal{L}(\tilde{g})$ can be determined by solving for the eigenvectors of

$$B_\mathcal{L}(\tilde{g}) = \boldsymbol{\Phi}_\mathcal{L}^H(\tilde{g})\boldsymbol{\Phi}_\mathcal{L}(\tilde{g}). \qquad (39)$$

Without exploiting the structure of the MCA matrix, forming $B_\mathcal{L}(\tilde{g}) \in \mathbb{C}^{M \times M}$ and computing its eigenvectors requires $O(NRM^2)$ operations. Using (35), the matrix product (39) can be expressed as

$$B_\mathcal{L}(\tilde{g}) = \sum_{j=1}^{R} C^T\{e_{l_j}\}\tilde{\boldsymbol{g}}^*\tilde{\boldsymbol{g}}^T C\{e_{l_j}\} \qquad (40)$$

where $\tilde{\boldsymbol{g}}^* = (\tilde{\boldsymbol{g}}^T)^H$ (i.e., all of the entries of $\tilde{\boldsymbol{g}}$ are conjugated). Let $\boldsymbol{H}(\tilde{g}) \stackrel{\text{def}}{=} \tilde{\boldsymbol{g}}^*\tilde{\boldsymbol{g}}^T$. The effect of $C^T\{e_{l_j}\}$ in (40) is to circularly shift $\boldsymbol{H}(\tilde{g})$ up by l_j pixels along each column, while $C\{e_{l_j}\}$ circularly shifts $\boldsymbol{H}(\tilde{g})$ to the left by l_j pixels along each row. Thus, $\boldsymbol{H}(\tilde{g})$ can be computed once initially, and then $B_\mathcal{L}(\tilde{g})$ can be formed by adding shifted versions of $\boldsymbol{H}(\tilde{g})$, which requires only $O(NM^2)$ operations. Thus, the computation has been reduced by a factor of R. In addition, the memory requirements have also been reduced by R times (assuming $M \approx N$), since only $\boldsymbol{H}(\tilde{g}) \in \mathbb{C}^{M \times M}$ needs to be stored, as opposed to $\boldsymbol{\Phi}_\mathcal{L}^H(\tilde{g}) \in \mathbb{C}^{NR \times M}$. As a result, the total cost of constructing $B_\mathcal{L}(\tilde{g})$ and performing its eigendecomposition is $O(NM^2)$ (when $M \leq N$).

V. APPLICATION OF SHARPNESS METRIC OPTIMIZATION TO MCA

A. Bringing Metrics to the MCA Framework

The vector space framework of the MCA approach allows sharpness metric optimization to be incorporated as a regularization procedure. The use of sharpness metrics can improve the solution when multiple singular values of $\mathbf{\Phi}_\Omega(\tilde{\mathbf{g}})$ are close to zero. In addition, metric optimization is beneficial in cases where the low-return assumption $|\xi[m,n]| \approx 0$ holds weakly, or where additive noise with large variance is present. In these non-ideal scenarios, we show how the MCA framework provides an approximate reduced-dimension solution subspace, where the optimization may be performed over a small set of parameters.

Suppose that instead of knowing that the image pixels in the low-return region are exactly zero, we can assume only that

$$\|\{\mathbf{vec}\{\mathbf{g}\}\}_\Omega\|_2^2 \le c \tag{41}$$

for some specific constant c. Then, the MCA condition becomes

$$\|\mathbf{\Phi}_\Omega(\tilde{\mathbf{g}})\mathbf{f}\|_2^2 \le c\|\mathbf{f}\|_2^2. \tag{42}$$

Note that the true correction filter $\mathbf{f}^\star$ must satisfy (42).

The goal of using sharpness optimization is to determine the best $\mathbf{f}$ (in the sense of producing an image with maximum sharpness) satisfying (42). We now derive a reduced-dimension subspace for performing the optimization where (42) holds for all $\mathbf{f}$ in the subspace. To accomplish this, we first determine σ_{M-K+1}, which we define as the largest singular value of $\mathbf{\Phi}_\Omega(\tilde{\mathbf{g}})$ satisfying $\sigma_k^2 \le c$. Then we express $\mathbf{f}$ in terms of the basis formed from the right singular vectors of $\mathbf{\Phi}_\Omega(\tilde{\mathbf{g}})$ corresponding to the K smallest singular values, i.e.,

$$\mathbf{f} = \sum_{k=M-K+1}^{M} v_k \tilde{\mathbf{V}}^{[k]} \tag{43}$$

where v_k is a basis coefficient corresponding to the basis vector $\tilde{\mathbf{V}}^{[k]}$. To demonstrate that every element of the K-dimensional subspace in (43) satisfies (42), we define $S_K^\star = \mathrm{span}\{\tilde{\mathbf{V}}^{[M-K+1]}, \tilde{\mathbf{V}}^{[M-K+2]}, \ldots, \tilde{\mathbf{V}}^{[M]}\}$, and note that [20]

$$\max_{\substack{\|\mathbf{f}\|_2=1 \\ \mathbf{f} \in S_K^\star}} \|\mathbf{\Phi}_\Omega(\tilde{\mathbf{g}})\mathbf{f}\|_2^2$$

$$= \max_{\substack{\|\mathbf{f}\|_2=1 \\ \mathbf{f} \in S_K^\star}} \|\tilde{\mathbf{U}}\mathbf{\Sigma}\tilde{\mathbf{V}}^H\mathbf{f}\|_2^2$$

$$= \max_{\substack{\|\mathbf{v}\|_2=1 \\ v_1=v_2=\cdots=v_{M-K}=0}} \|\mathbf{\Sigma}\mathbf{v}\|_2^2$$

$$= \max_{\|\mathbf{v}\|_2=1} \sum_{k=M-K+1}^{M} \sigma_k^2 |v_k|^2 = \sigma_{M-K+1}^2 \le c \tag{44}$$

where $\mathbf{v} \stackrel{\mathrm{def}}{=} \tilde{\mathbf{V}}^H \mathbf{f}$. In the second equality, the unitary property of $\tilde{\mathbf{V}}$ is used to obtain $\|\mathbf{f}\|_2 = \|\mathbf{v}\|_2$, and also $\mathbf{f} = \tilde{\mathbf{V}}\mathbf{v}$, from which it is observed that $\mathbf{f} \in S_K^\star$ implies $v_1 = v_2 = \cdots =$

$v_{M-K} = 0$. We note that the subspace $S_K^\star$ does not contain all $\mathbf{f}$ satisfying (42). However, it provides an optimal K-dimensional subspace in the following sense: for any subspace S_K where $\dim(S_K) = K$, we have [19]

$$\max_{\substack{\|\mathbf{f}\|_2=1 \\ \mathbf{f} \in S_K}} \|\mathbf{\Phi}_\Omega(\tilde{\mathbf{g}})\mathbf{f}\|_2^2 \ge \max_{\substack{\|\mathbf{f}\|_2=1 \\ \mathbf{f} \in S_K^\star}} \|\mathbf{\Phi}_\Omega(\tilde{\mathbf{g}})\mathbf{f}\|_2^2$$

$$= \sigma_{M-K+1}^2. \tag{45}$$

Thus, $S_K^\star$ is the best K-dimensional subspace in the sense that every element is feasible [i.e., satisfies (42)], and among all K-dimensional subspaces $S_K^\star$ minimizes the maximum energy in the low-return region.

Substituting the basis expansion (43) for $\mathbf{f}$ into (7) allows $\mathbf{g}$ to be expressed in terms of an approximate reduced-dimension basis

$$\mathbf{g_d} = \sum_{k=1}^{K} d_k \boldsymbol{\psi}^{[k]} \tag{46}$$

where

$$\boldsymbol{\psi}^{[k]} = C\{\tilde{\mathbf{V}}^{[M-K+k]}\}\tilde{\mathbf{g}} \tag{47}$$

$d_k = v_{M-K+k}$, and $\mathbf{g_d}$ is the image parameterized by the basis coefficients $\mathbf{d} = [d_1, d_2, \ldots, d_K]^T$. To obtain the best $\hat{\mathbf{g}}$ that satisfies the data consistency condition, we optimize a particular sharpness metric over the coefficients $\mathbf{d}$, where the number of coefficients $K \ll M$.

B. Performing the Metric Optimization

We define the metric objective function $\mathcal{C} : \mathbb{C}^K \to \mathbf{R}$ as the mapping from the basis coefficients $\mathbf{d} = [d_1, d_2, \ldots, d_K]^T$ to a sharpness cost

$$\mathcal{C}(\mathbf{d}) = \sum_{m=0}^{M-1} \sum_{n=0}^{N-1} S(\bar{I}_{\mathbf{d}}[m,n]) \tag{48}$$

where $I_{\mathbf{d}}[m,n] = |g_{\mathbf{d}}[m,n]|^2$ is the intensity of each pixel, $\bar{I}_{\mathbf{d}}[m,n] = I_{\mathbf{d}}[m,n]/\gamma_{\mathbf{g_d}}$ is the normalized intensity with $\gamma_{\mathbf{g_d}} = \|\mathbf{g_d}\|_2^2$, and $S : \mathbf{R}^+ \to \mathbf{R}$ is an image sharpness metric operating on the normalized intensity of each pixel. An example of a commonly used sharpness metric in SAR is the image entropy: $S_H(\bar{I}_{\mathbf{d}}[m,n]) \stackrel{\mathrm{def}}{=} -\bar{I}_{\mathbf{d}}[m,n]\ln \bar{I}_{\mathbf{d}}[m,n]$ [5], [6]. A gradient-based search can be used to determine a local minimizer of $\mathcal{C}(\mathbf{d})$ [21]. The kth element of the gradient $\nabla_{\mathbf{d}}\mathcal{C}(\mathbf{d})$ is determined using

$$\frac{\partial \mathcal{C}(\mathbf{d})}{\partial d_k} = \sum_{m,n} \frac{\partial S(\bar{I}_{\mathbf{d}}[m,n])}{\partial \bar{I}_{\mathbf{d}}[m,n]} \left(\frac{2}{\gamma_{\mathbf{g_d}}} g_{\mathbf{d}}[m,n]\psi^{*[k]}[m,n] \right.$$

$$\left. - \frac{2}{\gamma_{\mathbf{g_d}}^2} I_{\mathbf{d}}[m,n] \sum_{m',n'} g_{\mathbf{d}}[m',n']\psi^{*[k]}[m',n'] \right) \tag{49}$$

where $*$ denotes the complex conjugate. Note that (49) can be applied to a variety of sharpness metrics. Considering the entropy example, the derivative of the sharpness metric is $\partial S_H(\bar{I}_{\mathbf{d}}[m,n])/\partial \bar{I}_{\mathbf{d}}[m,n] = -(1 + \ln \bar{I}_{\mathbf{d}}[m,n])$.

VI. SAR Data Acquisition and Processing

In this section, we discuss the application of the MCA technique in practical scenarios. One way of satisfying the image support assumption used in MCA is to exploit the SAR antenna pattern. In spotlight-mode SAR, the area of terrain that can be imaged depends on the *antenna footprint*, i.e., the illuminated portion of the scene corresponding to the projection of the antenna main-beam onto the ground plane [1]. There is low return from features outside of the antenna footprint. The fact the SAR image is essentially spatially limited, due to the profile of the antenna beam pattern, suggests that the proposed autofocus technique can be applied in spotlight-mode SAR imaging given that the SAR data are sampled at a sufficiently high rate [1], [22], [23].

The amount of area represented in a SAR image, the image *field of view* (FOV), is determined by how densely the analog Fourier transform is sampled. As the density of the sampling is increased, the FOV of the image increases. For a spatially limited scene, there is a critical sampling density at which the image coverage is equal to the support of the scene (determined by the width of the antenna footprint). If the Fourier transform is sampled above the critical rate, the FOV of the image extends beyond the finite support of the scene, and the result resembles a zero-padded or zero-extended image. Our goal is to select the Fourier domain sampling density such that the FOV of the SAR image extends beyond the brightly illuminated portion of the scene. In doing so, we cause the perfectly focused digital image to be (effectively) spatially limited, allowing the use of the proposed autofocus approach.

Fig. 3 shows an illustration of the antenna pattern along the x-axis. A length $\mathcal{X}'$ region of the scene is brightly illuminated in the x dimension. To use the MCA approach to autofocus, we need the image coverage $\mathcal{X}$ to be greater than the illuminated region $\mathcal{X}'$. To model the antenna pattern, we consider the case of an unweighted uniformly radiating antenna aperture. Under this scenario, both the transmit and receive patterns are described by a sinc function [24]–[26]. Thus, the antenna footprint determined by the combined transmit-receive pattern is modeled as [1], [24]

$$w(x) = \text{sinc}^2(W_x^{-1} x) \tag{50}$$

where

$$W_x = \frac{\lambda_0 R_0}{D} \tag{51}$$

$\text{sinc}(x) \overset{\text{def}}{=} (\sin \pi x)/(\pi x)$, x is the cross-range coordinate, λ_0 is the wavelength of the radar, R_0 is the range from the radar platform to the center of the scene, and D is the length of the antenna aperture. Near the nulls of the antenna pattern at $x = \pm W_x$, the attenuation will be very large, producing low-return rows in the perfectly focused SAR image consistent with (29).

Using the model in (50), the Fourier-domain sampling density should be large enough so that the FOV of the SAR image is equal to or greater than the width of the mainlobe of the sinc window: $\mathcal{X} \geq 2W_x$. In spotlight-mode SAR, the Fourier-domain sampling density in the cross-range dimension is determined by the pulse repetition frequency (PRF) of the radar.
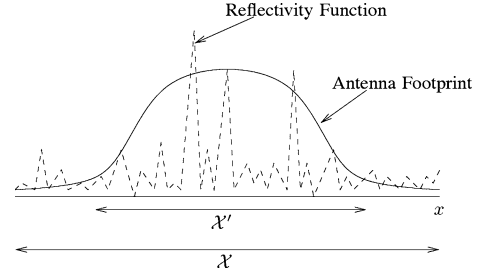

Fig. 3. Antenna pattern shown superimposed on the scene reflectivity function for a single range (y) coordinate. The finite beamwidth of the antenna causes the terrain to be illuminated only within a spatially limited window; the return outside the window is near zero.

For a radar platform moving with constant velocity, increasing the PRF decreases the angular interval between pulses (i.e., the angular increment between successive look angles), thus increasing the cross-range Fourier-domain sampling density and FOV [1], [23], [24]. Alternatively, keeping the PRF constant and decreasing the platform velocity also increases the cross-range Fourier-domain sampling density; such is the case in airborne SAR when the aircraft is flying into a headwind. In many cases, the platform velocity and PRF are such that the image FOV is approximately equal to the mainlobe width of (50); in these cases, the final images are usually cropped to half the mainlobe width of the sinc window [1], because it is realized that the edge of the processed image will suffer from some amount of aliasing. Our framework suggests that the additional information from the disgarded portions of the image can be used for SAR image autofocus.

Another instance where the image support assumption can be exploited is when prior knowledge of low-return features in the SAR image is available. Examples of such features include smooth bodies of water, roads, and shadowy regions [5]. If the image defocusing is not very severe, then low-return regions can be estimated using the defocused image. Inverse SAR (ISAR) provides a further application for MCA. In ISAR images, pixels outside of the support of the imaged object (e.g., aircraft) correspond to a region of *zero* return [5]. Thus, given an estimate of the object support, MCA can be applied.

VII. Experimental Results

Fig. 4 presents an experiment using an actual SAR image. To form a ground truth perfectly focused image, an entropy-minimization autofocus routine [6] was applied to the given SAR image. Fig. 4(a) shows the resulting image, where the sinc-squared window in Fig. 4(b) has been applied to each column to simulate the antenna footprint resulting from an unweighted antenna aperture. The cross-range FOV equals 95 percent of the mainlobe width of the squared-sinc function, i.e., the image is cropped within the nulls of the antenna footprint, so that there is very large (but not infinite) attenuation at the edges of the image. Fig. 4(c) shows a defocused image produced by applying a white phase error function (i.e., independent phase components uniformly distributed between $-\pi$ and π) ϕ_e to the perfectly focused image in Fig. 4(a) according to (1); the application of white phase error functions has been considered previously in the autofocus literature as a particularly stressing case
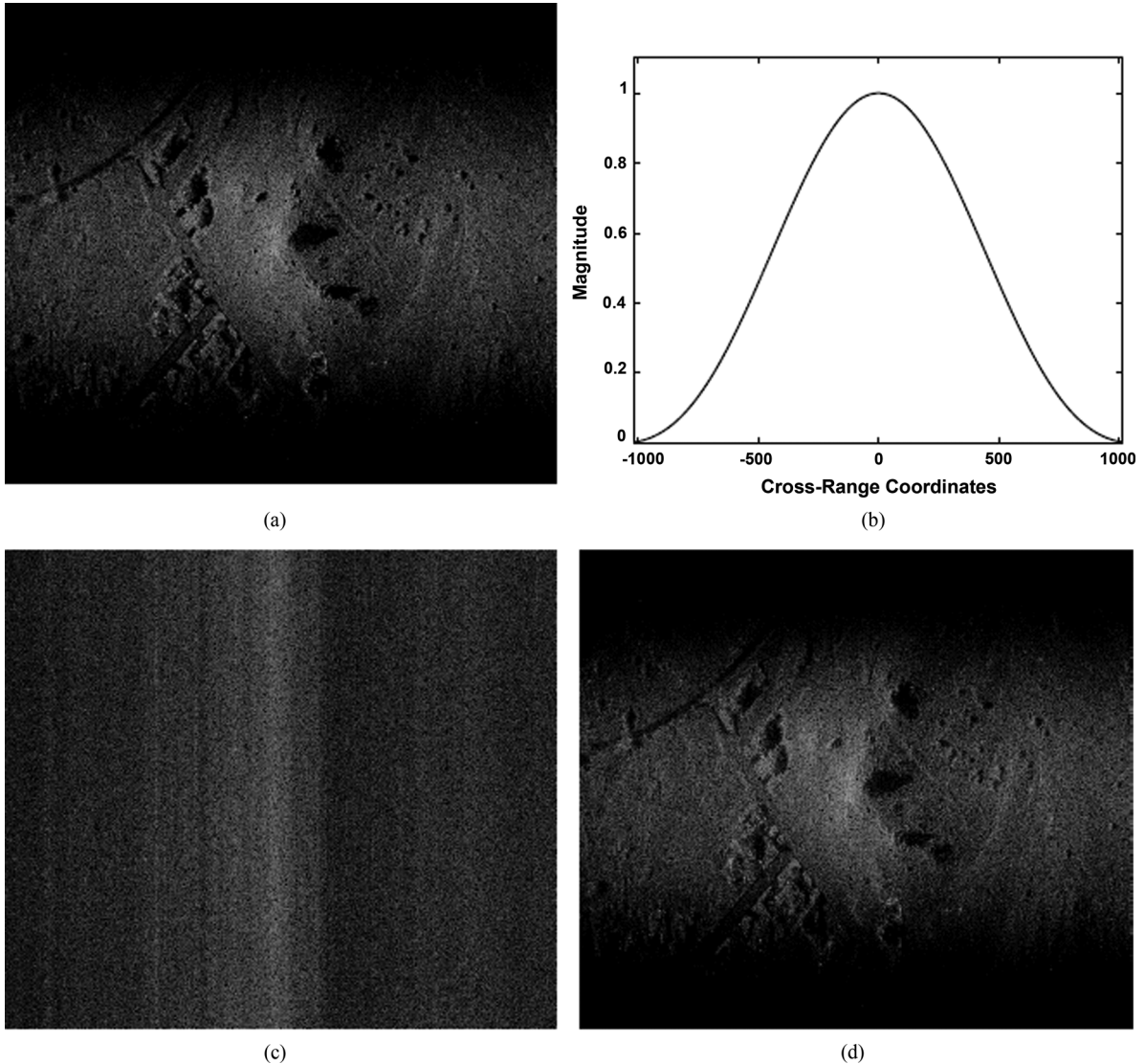
Fig. 4. Actual 2335×2027 pixel SAR image: (a) Perfectly focused image, where the simulated sinc-squared antenna footprint in (b) has been applied to each column, (c) defocused image produced by applying a white phase error function, and (d) MCA restoration ($\mathrm{SNR_{out}} = 10.52$ dB).

to test the robustness of autofocus algorithms[4], [5], [27]. We applied MCA to the defocused image assuming the top and bottom rows of the perfectly focused image to be low-return. The MCA restoration is displayed in Fig. 4(d). The restored image is observed to be in good agreement with the ground truth image. To quantitatively assess the performance of autofocus techniques, we use the restoration quality metric $\mathrm{SNR_{out}}$ (i.e., *output signal-to-noise ratio*), which is defined as [28]

$$\mathrm{SNR_{out}} = 20 \log_{10} \frac{\left\| \mathbf{vec}\{\boldsymbol{g}\} \right\|_2}{\left\| (|\mathbf{vec}\{\boldsymbol{g}\}| - |\mathbf{vec}\{\hat{\boldsymbol{g}}\}|) \right\|_2}$$

here, the "noise" in $\mathrm{SNR_{out}}$ refers to the error in the magnitude of the reconstructed image $\hat{\boldsymbol{g}}$ relative to the perfectly focused image $\boldsymbol{g}$, and should not be confused with additive noise (which is considered later). For the restoration in Fig. 4(d), $\mathrm{SNR_{out}} = 10.52$ dB.

To evaluate the robustness of MCA with respect to the low-return assumption, we performed a series of experiments using the idealized window function in Fig. 5(a). The window has a flat response over most of the image; the tapering at the edges of the window is described by a quarter-period of a sine function. In each experiment, the *gain* at the edges of the window (i.e., the inverse of the attenuation) is increased such that the pixel magnitudes in the low-return region (corresponding to the top and bottom rows) become larger. In Fig. 5(a), a window gain of 0.1 is shown. For each value of the window gain, a defocused image is formed and the MCA restoration is produced.

Fig. 5(b) shows a plot of the restoration quality metric $\mathrm{SNR_{out}}$ versus the gain at the edges of the window, where the top two rows and bottom two rows are assumed to be low-return. The simulated SAR image in Fig. 5(c) was used as the ground truth perfectly focused image in this set of experiments; here, a processed SAR image[1] is used as a model for the image magnitude, while the phase of each pixel is selected at random (uniformly distributed between $-\pi$ and π and uncorrelated) to simulate the complex reflectivity associated with high

[1]The processed SAR images in this paper were provided by Sandia National Laboratories.
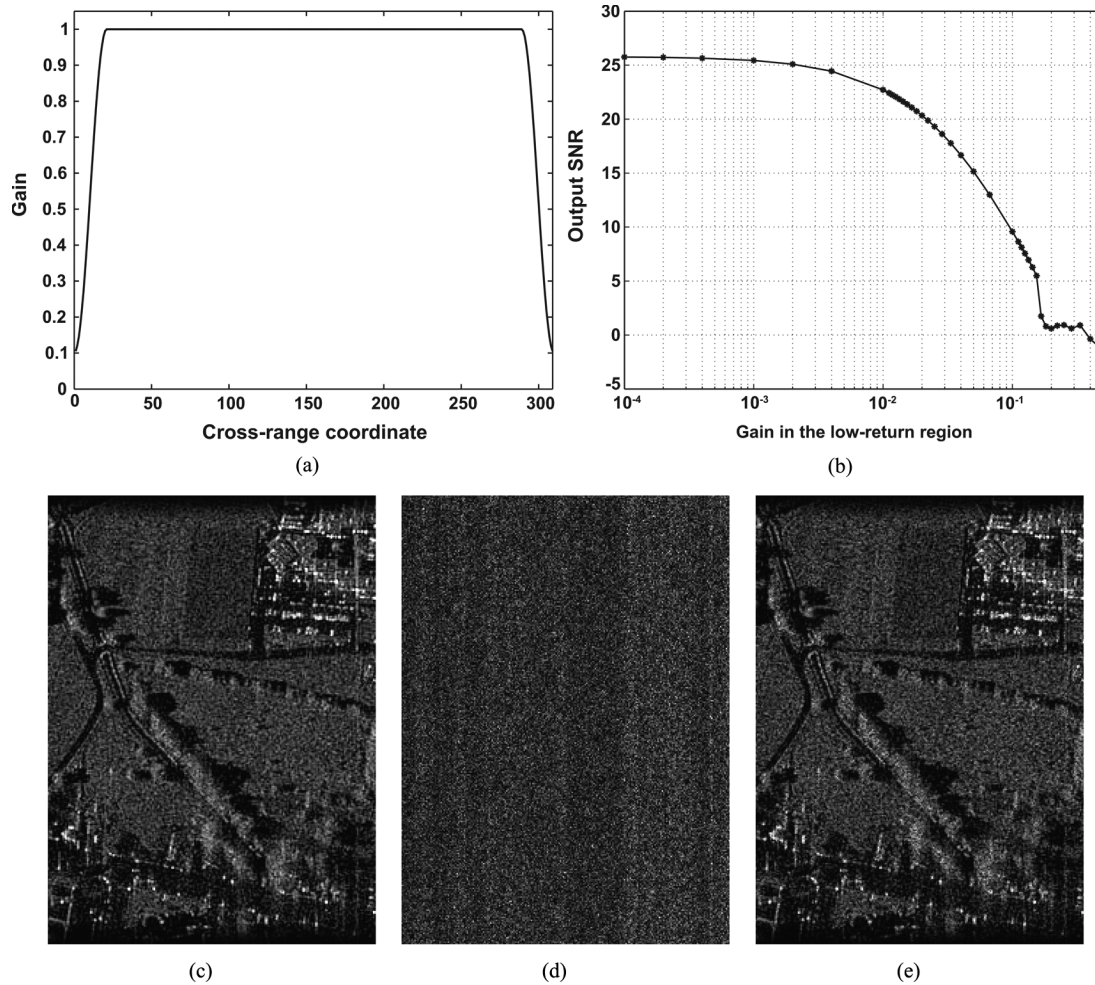
Fig. 5. Experiments evaluating the robustness of MCA as a function of the attenuation in the low-return region: (a) Window function applied to each column of the SAR image, where the gain at the edges of the window (corresponding to the low-return region) is varied with each experiment (a gain of 0.1 is shown); (b) plot of the quality metric $\mathrm{SNR}_{\mathrm{out}}$ for the MCA restoration (measured with respect to the perfectly focused image) versus the window gain in the low-return region; (c) simulated perfectly focused 309 by 226 pixel image, where the window in (a) has been applied; (d) defocused image produced by applying a white phase error function; and (e) MCA restoration ($\mathrm{SNR}_{\mathrm{out}} = 9.583$ dB).

frequency SAR images of terrain [29]. The plot in Fig. 5(b) demonstrates that the restoration quality decreases monotonically as a function of increasing window gain. We observe that for values of $\mathrm{SNR}_{\mathrm{out}}$ less than 3 dB, the restored images do not resemble the perfectly focused image; this transition occurs when gain in the low-return region increases above 0.14. For gain values less than or equal to 0.14, the restorations are faithful representations of the perfectly focused image. Thus, we see that MCA is robust over a large range of attenuation values, even when there is significant deviation from the ideal zero-magnitude pixel assumption. As an example, the MCA restoration in Fig. 5(e) corresponds to an experiment where the window gain is 0.1. Fig. 5(c) and (d) shows the perfectly focused and defocused images, respectively, associated with this restoration. The image in Fig. 5(e) is almost perfectly restored, with $\mathrm{SNR}_{\mathrm{out}} = 9.583$ dB.

In Fig. 6, the performance of MCA is compared with existing autofocus approaches. Fig. 6(a) shows a perfectly focused simulated SAR image, constructed in the same manner as Fig. 5, where the window function in Fig. 5(b) has been applied (the window gain is 1×10^{-4} in this experiment). A defocused

image formed by applying a quadratic phase error function (i.e., the phase error function varies as a quadratic function of the cross-range frequencies) is displayed in Fig. 6(b); such a function is used to model phase errors due to platform motion [1]. The defocused image has been contaminated with additive white complex-Gaussian noise in the range-compressed domain such that the *input signal-to-noise ratio* (input SNR) is 40 dB; here, the input SNR is defined to be the average per-pulse SNR: $\mathrm{SNR} = 20 \log_{10}\{1/M \sum_k \max_n |\tilde{G}[k,n]|/\sigma_p\}$, where σ_p is the noise standard deviation. Fig. 6(c) shows the MCA restoration formed assuming the top two and bottom two rows to be low-return; the image is observed to be well-restored, with $\mathrm{SNR}_{\mathrm{out}} = 25.25$ dB. To facilitate a meaningful comparison with the perfectly focused image, the restorations are produced by applying the phase error estimate to the *noiseless* defocused image; in other words, the phase estimate is determined in the presence of noise, but $\mathrm{SNR}_{\mathrm{out}}$ is computed with the noise removed. A restoration produced using PGA is displayed in Fig. 6(d) ($\mathrm{SNR}_{\mathrm{out}} = 9.64$ dB) [1]. Fig. 6(e) and (f) shows the result of applying a metric-based autofocus technique [6] using the entropy sharpness metric ($\mathrm{SNR}_{\mathrm{out}} = 3.60$ dB) and
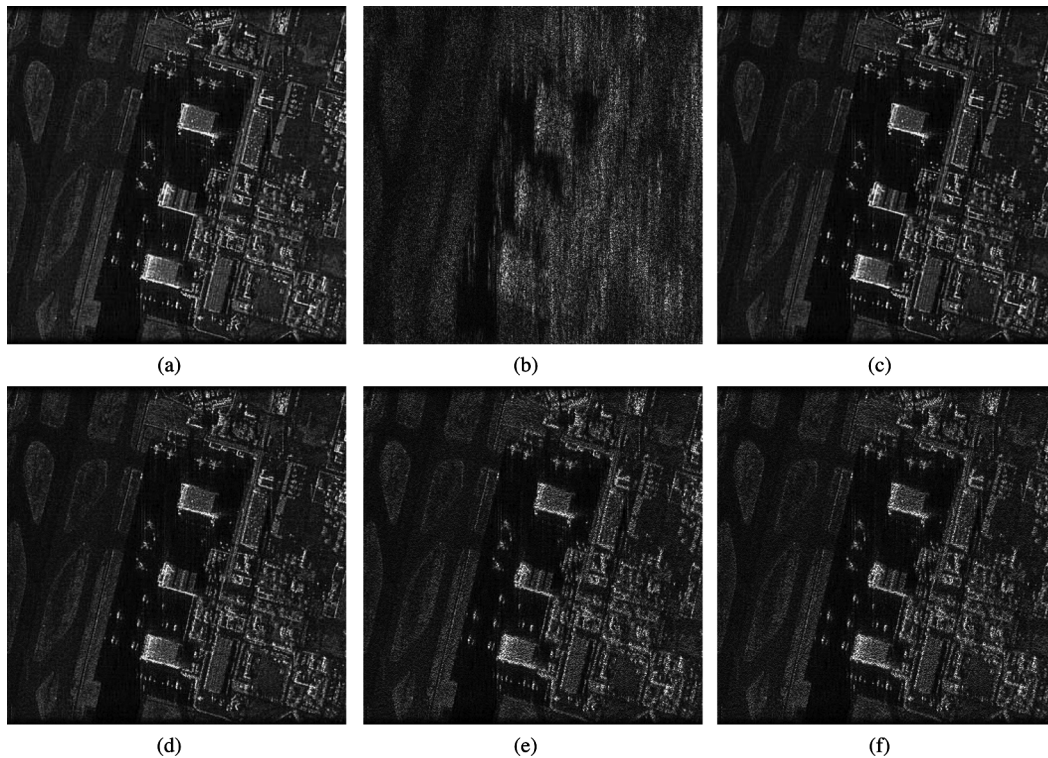
Fig. 6. Comparison of MCA with existing autofocus approaches: (a) Simulated 341 by 341 pixel perfectly focused image, where the window function in Fig. 5(b) has been applied; (b) noisy defocused image produced by applying a quadratic phase error, where the input SNR is 40 dB (measured in the range-compressed domain); (c) MCA restoration ($\mathrm{SNR_{out}} = 25.25$ dB); (d) PGA restoration ($\mathrm{SNR_{out}} = 9.64$ dB); (e) entropy-based restoration ($\mathrm{SNR_{out}} = 3.60$ dB); and (f) restoration using the intensity-squared sharpness metric ($\mathrm{SNR_{out}} = 3.41$ dB).

the intensity-squared sharpness metric ($\mathrm{SNR_{out}} = 3.41$ dB), respectively. Of the four autofocus approaches, MCA is found to produce the highest quality restoration in terms of both qualitative comparison and the quality metric $\mathrm{SNR_{out}}$. In particular, the metric-based restorations, while macroscopically similar to the MCA and PGA restorations, have much lower SNR; this is due to the metric-based techniques incorrectly accentuating some of the point scatterers.

Fig. 7 presents the results of a Monte Carlo simulation comparing the performance of MCA with existing autofocus approaches under varying levels of additive noise. Ten trials were conducted at each input SNR level, where in each trial a noisy defocused image (using a deterministic quadratic phase error function) was formed using different randomly generated noise realizations with the same statistics. Four autofocus approaches (MCA, PGA, entropy-minimization, and intensity-squared minimization) were applied to each defocused image, and the quality metric $\mathrm{SNR_{out}}$ was evaluated on the resulting restorations. Plots of the average $\mathrm{SNR_{out}}$ (over the ten trials) versus the input SNR are displayed in Fig. 7 for the four autofocus methods. The plot shows that at high input SNR ($\mathrm{SNR} \geq 20$ dB), MCA provides the best restoration performance. At very low SNR, metric-based methods produce the highest $\mathrm{SNR_{out}}$; however, this performance is observed to level out around 3.5 dB due to the limitation of the sharpness criterion (several point scatterers are artificially accentuated). PGA provides the best performance in the intermediate range of low SNR starting around 13 dB. Likewise, we observe that the MCA restorations start to resemble the perfectly focused
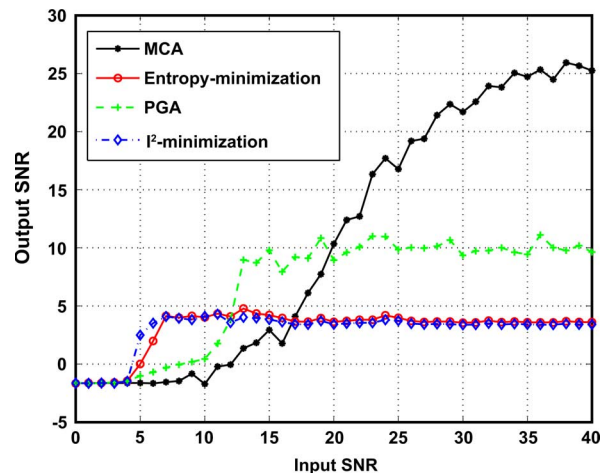

Fig. 7. Plots of the restoration quality metric $\mathrm{SNR_{out}}$ versus the input SNR for MCA, PGA, entropy-minimization autofocus, and intensity-squared minimization autofocus. In this experiment, we performed a Monte Carlo simulation where MCA was applied to noisy versions of the defocused image in Fig. 6(b); ten different white complex-Gaussian noise realizations were used for each experiment at a particular input SNR.

image at 13 dB. PGA also approaches a constant $\mathrm{SNR_{out}}$ value at high input SNR; the limitation in PGA is the inability to extract completely isolated point scatterers free of surrounding clutter.

On average, the MCA restorations in the experiment of Fig. 7 required 3.85 s of computation time, where the algorithm was implemented using MATLAB on an Intel Pentium 4
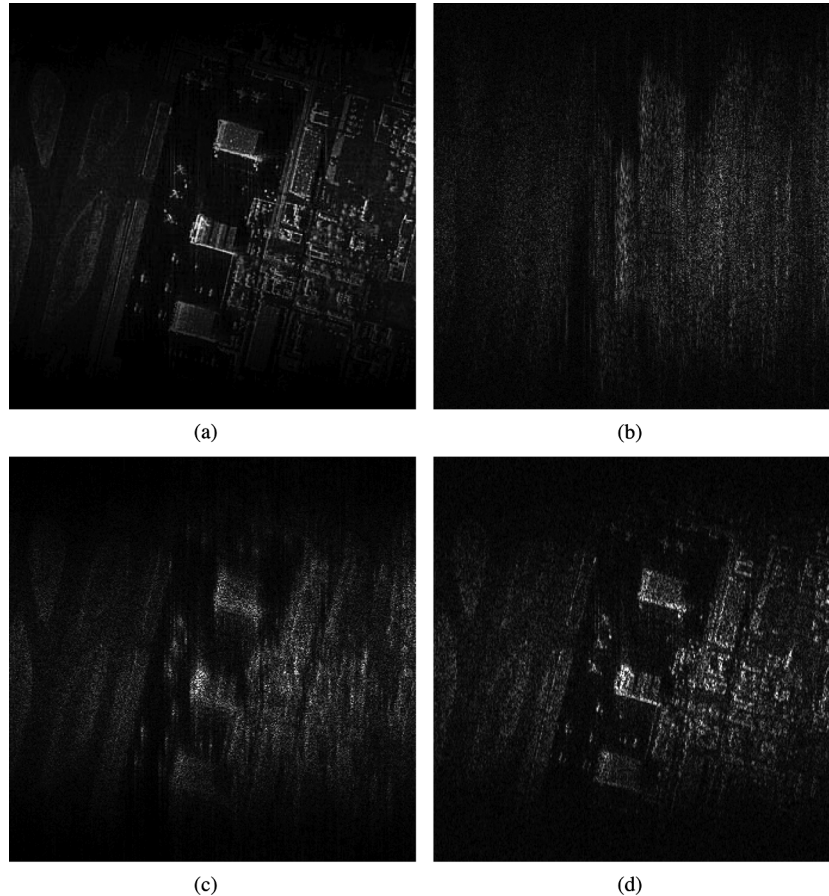
Fig. 8. Experiment using entropy optimization as a regularization procedure to improve the MCA restoration when the input SNR is low. The optimization is performed over a space of 15 basis functions determined by the smallest singular values of the MCA matrix. (a) Perfectly focused image where a sinc-squared window is applied, (b) noisy defocused image with range-compressed domain SNR of 19 dB produced using a quadratic phase error, (c) MCA restoration, and (d) regularized MCA restoration using the entropy metric.

CPU (2.66 GHz). In comparison, PGA, the intensity-squared approach, and the entropy approach had average run-times of 5.34, 18.1, and 87.6 s, respectively. Thus, MCA is observed to be computationally efficient in comparison with existing SAR autofocus methods.

Fig. 8 presents an experiment using a sinc-squared antenna pattern, where a significant amount of additive noise has been applied to the defocused image. The perfectly focused and defocused images are displayed in Fig. 8(a) and (b), respectively, where the input SNR of the defocused image is 19 dB. Due to the gradual tapering of the sinc-squared antenna pattern, the smallest singular values of the MCA matrix are distributed closely together. As a result, the problem becomes poorly conditioned in the sense that small perturbations to the defocused image can produce large perturbations to the least-squares solution of (20). In such cases, regularization can be used to improve the solution, as described in Section V. Fig. 8(c) shows the MCA restoration where a large number of low-return constraints (45 low-return rows at the top and bottom of the image) are enforced to improve the solution in the presence of noise. In this restoration, much of the defocusing has been corrected, revealing the structure of the underlying image. However, residual blurring remains. Fig. 8(d) shows the result of applying the regularization procedure in Section V. Here,

we form a subspace of 15 basis functions using the minimum right singular vectors of the MCA matrix where the data consistency relation (42) is satisfied. The optimal basis coefficients, corresponding to a unique solution within this subspace, are determined by minimizing the entropy metric. The regularized restoration is shown in Fig. 8(d). The incorporation of the entropy-based sharpness optimization is found to significantly improve the quality of the restoration, producing a result that agrees well with the perfectly focused image. Thus, by exploiting the linear algebraic structure of the SAR autofocus problem and the low-return constraints in the perfectly focused image, the dimension of the optimization space in metric-based methods can be greatly reduced (from 341 to 15 parameters in this example).

The simulations in this paper assume that the Fourier imaging data lie on a Cartesian grid. Further work is needed to determine how well MCA works for large data angles where the polar grid deviates substantially from Cartesian. Recent work suggests that the proposed MCA scheme should be modified for larger data angles [30].

VIII. CONCLUSION

In this paper, we have proposed a new subspace-based approach to the synthetic aperture radar (SAR) autofocus problem,

termed the MultiChannel Autofocus (MCA) algorithm. In this approach, an image focusing operator is determined directly using a linear algebraic formulation. Assuming that a small portion of the perfectly focused image is zero-valued, or corresponds to a region of low return, near-perfect restorations of the focused image are possible without requiring prior assumptions about the underlying scene; the success of existing autofocus approaches tends to rely on the accuracy of such prior assumptions, such as the suitability of image sharpness metrics or the presence of isolated point scatterers. In practice, the desired image support condition can be achieved by exploiting the spatially limited nature of the illuminating antenna beam.

The MCA approach is computationally efficient, and robust in the presence of noise and deviations from the ideal image support assumption. The restoration quality of the proposed method is independent of the severity of the phase error function; existing autofocus approaches sometimes perform poorly when the phase errors are large and rapidly varying. In addition, the vector-space formulation of MCA allows sharpness metric optimization to be incorporated into the restoration framework as a regularization term, enabling SAR autofocus to be cast into a more unified paradigm with other image restoration problems. Here, the parameter set over which the optimization is performed is greatly reduced in comparison to the number of unknown phase error components. We have presented experimental results, using actual and simulated SAR images, demonstrating that the proposed technique can produce superior restorations in comparison with existing autofocus approaches.

ACKNOWLEDGMENT

REFERENCES

[1] C. V. Jakowatz, Jr., D. E. Wahl, P. H. Eichel, D. C. Ghiglia, and P. A. Thompson, *Spotlight-Mode Synthetic Aperture Radar: A Signal Processing Approach*. Boston, MA: Kluwer, 1996.

[2] P. H. Eichel, D. C. Ghiglia, and C. V. Jakowatz, Jr., "Speckle processing method for synthetic-aperture-radar phase correction," *Opt. Lett.*, vol. 14, no. 1, pp. 1101–1103, Jan. 1989.

[3] C. V. Jakowatz, Jr. and D. E. Wahl, "Eigenvector method for maximum-likelihood estimation of phase errors in synthetic-aperture-radar imagery," *J. Opt. Soc. Amer. A*, vol. 10, no. 12, pp. 2539–2546, Dec. 1993.

[4] L. Xi, L. Guosui, and J. Ni, "Autofocusing of ISAR images based on entropy minimization," *IEEE Trans. Aerosp. Electron. Syst.*, vol. 35, no. 10, pp. 1240–1252, Oct. 1999.

[5] J. R. Fienup and J. J. Miller, "Aberration correction by maximizing generalized sharpness metrics," *J. Opt. Soc. Amer. A*, vol. 20, no. 4, pp. 609–620, Apr. 2003.

[6] T. J. Kragh, "Monotonic iterative algorithm for minimum-entropy autofocus," presented at the Adaptive Sensor Array Processing (ASAP) Workshop, Lexington, MA, Jun. 2006.

[7] F. Berizzi and G. Corsini, "Autofocusing of inverse synthetic aprture radar images using contrast optimization," *IEEE Trans. Aerosp. Electron. Syst.*, vol. 32, no. 7, pp. 1185–1191, Jul. 1996.

[8] W. D. Brown and D. C. Ghiglia, "Some methods for reducing propagation-induced phase errors in coherent imaging systems—I: Formalism," *J. Opt. Soc. Amer. A*, vol. 5, pp. 924–942, 1988.

[9] D. C. Ghiglia and W. D. Brown, "Some methods for reducing propagation-induced phase errors in coherent imaging systems—II: Numerical results," *J. Opt. Soc. Amer. A*, vol. 5, pp. 943–957, 1988.

[10] C. E. Mancill and J. M. Swiger, "A map drift autofocus technique for correcting higher-order SAR phase errors," in *Proc. 27th Annu. Tri-Service Radar Symp.*, Monterey, CA, Jun. 1981, pp. 391–400.

[11] R. G. Paxman and J. C. Marron, "Aberration correction of speckled imagery with an image sharpness criterion," presented at the SPIE Statistical Optics, San Diego, CA, 1988.

[12] R. L. Morrison, Jr. and D. C. Munson, Jr., "An experimental study of a new entropy-based SAR autofocus technique," in *Proc. IEEE Int. Conf. Image Processing*, Rochester, NY, 2008, vol. II, pp. 441–444.

[13] L. Tong and S. Perreau, "Multichannel blind identification: From subspace to maximum likelihood methods," *Proc. IEEE*, vol. 86, no. 10, pp. 1951–1968, Oct. 1998.

[14] M. Gurelli and C. Nikias, "EVAM: An eigenvector-based algorithm for multichannel blind deconvolution of input colored signals," *IEEE Trans. Signal Process.*, vol. 43, 1, no. 1, pp. 134–149, Jan. 1995.

[15] G. Harikumar and Y. Bresler, "Blind restoration of images blurred by multiple filters: Theory and efficient algorithms," *IEEE Trans. Image Process.*, vol. 8, no. 2, pp. 202–219, Jun. 1999.

[16] R. L. Morrison, Jr. and M. N. Do, "A multichannel approach to metric-based SAR autofocus," in *Proc. IEEE Int. Conf. Image Processing*, Genoa, Italy, 2005, vol. 2, pp. 1070–1073.

[17] R. L. Morrison, Jr. and M. N. Do, "Multichannel autofocus algorithm for synthetic aperture radar," presented at the IEEE Int. Conf. Image Processing, Atlanta, GA, 2006.

[18] R. L. Morrison, Jr., M. N. Do, and D. C. Munson, Jr., "SAR image autofocus by sharpness optimization: A theoretical study," *IEEE Trans. Image Process.*, vol. 16, no. 9, pp. 2309–2321, Sep. 2007.

[19] G. H. Golub and C. F. Van Loan, *Matrix Computations*. Baltimore, MD: Johns Hopkins Univ. Press, 1996.

[20] R. A. Horn and C. R. Johnson, *Matrix Analysis*. New York: Cambridge Univ. Press, 2005.

[21] D. G. Luenberger, *Linear and Nonlinear Programming*. Boston, MA: Kluwer, 2003.

[22] J. Walker, "Range-doppler imaging of rotating objects," *IEEE Trans. Aerosp. Elctron. Syst.*, vol. AES-16, no. 1, pp. 23–52, Jan. 1980.

[23] D. C. Munson, Jr., J. D. O'Brien, and W. K. Jenkins, "A tomographic formulation of spotlight-mode synthetic aperture radar," *Proc. IEEE*, vol. 71, no. , pp. 917–925, Aug. 1983.

[24] M. Soumekh, *Synthetic Aperture Radar Signal Processing with MATLAB Algorithms*. New York: Wiley, 1999.

[25] R. E. Blahut, *Theory of Remote Image Formation*. Cambridge, U.K.: Cambridge Univ. Press, 2004.

[26] M. I. Skolnik, *Introduction to Radar Systems*. New York: McGraw-Hill, 2002.

[27] D. E. Wahl, P. H. Eichel, D. C. Ghiglia, and C. V. Jakowatz, Jr., "Phase gradient autofocus—A robust tool for high resolution SAR phase correction," *IEEE Trans. Aerosp. Electron. Syst.*, vol. 30, no. 7, pp. 827–835, Jul. 1994.

[28] M. Vetterli and J. Kovacevic, *Wavelets and Subband Coding*. Englewood Cliffs, NJ: Prentice-Hall, 1995.

[29] D. C. Munson, Jr. and J. L. C. Sanz, "Image reconstruction from frequency-offset Fourier data," *Proc. IEEE*, vol. 72, no. 6, Jun. 1984.

[30] H. J. Cho and D. C. Munson, Jr., "Overcoming polar format issues in multichannel SAR autofocus," presented at the 42nd Asilomar Conf. Signals, Systems, and Computers, Monterey, CA, Oct. 2008.

Robert L. Morrison, Jr. (S'02–M'07) was born in Voorhees, NJ, in 1977. He received the B.S.E. degree in electrical engineering from the University of Iowa in 2000, and the M.S. and Ph.D. degrees in electrical engineering from the University of Illinois at Urbana-Champaign, Urbana, in 2002 and 2007, respectively.

He is currently a member of the technical staff at the Massachusetts Institute of Technology Lincoln Laboratory, Lexington. His research interests include radar imaging, medical imaging, and signal processing.

Minh N. Do (M'01–SM'07) was born in Thanh Hoa, Vietnam, in 1974. He received the B.Eng. degree in computer engineering from the University of Canberra, Australia, in 1997, and the Dr.Sci. degree in communication systems from the Swiss Federal Institute of Technology Lausanne (EPFL), Switzerland, in 2001.

Since 2002, he has been on the faculty at the University of Illinois at Urbana-Champaign (UIUC), Urbana, where he is currently an Associate Professor in the Department of Electrical and Computer Engineering and holds joint appointments with the Coordinated Science Laboratory and the Beckman Institute for Advanced Science and Technology. His research interests include image and multidimensional signal processing, wavelets and multiscale geometric analysis, computational imaging, and visual information representation.

Prof. Do received a Silver Medal from the 32nd International Mathematical Olympiad in 1991, a University Medal from the University of Canberra in 1997, the best doctoral thesis award from EPFL in 2001, and a CAREER award from the National Science Foundation in 2003. He was named a Beckman Fellow at the Center for Advanced Study, UIUC, in 2006, and received a Xerox Award for Faculty Research from the College of Engineering, UIUC, in 2007. He is a member of the IEEE Signal Processing Society Signal Processing Theory and Methods and Image and MultiDimensional Signal Processing Technical Committees and an Associate Editor of the IEEE TRANSACTIONS ON IMAGE PROCESSING.

David C. Munson, Jr. (S'74–M'79–SM'84–F'91) received the B.S. degree in electrical engineering (with distinction) from the University of Delaware, Newark, in 1975, and the M.S., M.A., and Ph.D. degrees in electrical engineering from Princeton University, Princeton, NJ, in 1977, 1977, and 1979, respectively.

From 1979 to 2003, he was with the University of Illinois at Urbana-Champaign, Urbana, where he was the Robert C. MacClinchie Distinguished Professor of Electrical and Computer Engineering, Research Professor in the Coordinated Science Laboratory, and a faculty member in the Beckman Institute for Advanced Science and Technology. In 2003, he became Chair of the Department of Electrical Engineering and Computer Science at the University of Michigan, Ann Arbor. He is currently the Robert J. Vlasic Dean of Engineering at the University of Michigan. His teaching and research interests are in the general area of signal and image processing. His research is focused on radar imaging, passive millimeter-wave imaging, and computer tomography. He has held summer industrial positions in digital communications and speech processing, and he has served as a consultant in synthetic aperture radar. He is the co-founder of InstaRecon, Inc., a start-up to commercialize fast algorithms for image formation in computer tomography. He is affiliated with the Infinity Project, where he is coauthor of a textbook on the digital world, which is used in high schools nationwide to introduce students to engineering.

Prof. Munson is a Fellow of the Institute of Electrical and Electronics Engineers (IEEE), a past president of the IEEE Signal Processing Society, founding Editor-in-Chief of the IEEE TRANSACTIONS ON IMAGE PROCESSING, and co-founder of the IEEE International Conference on Image Processing. In addition to multiple teaching awards and other honors, he was presented the Society Award of the IEEE Signal Processing Society, he served as a Distinguished Lecturer of the IEEE Signal Processing Society, he received an IEEE Third Millennium Medal, and he was the Texas Instruments Distinguished Visiting Professor at Rice University.